Oblique scattering from non-Hermitian optical waveguides

Tal Goldstein and Gal Shmuel
Faculty of Mechanical Engineering, Technion–Israel Institute of Technology, Haifa 32000, Israel

(Received 10 October 2022; accepted 20 January 2023; published 6 February 2023)

A judicious design of gain and loss leads to counterintuitive wave phenomena that are inaccessible by conservative systems. Notably, such designs can give rise to laser-absorber modes and anisotropic transmission resonances. Here, we analyze the emergence of these phenomena in an optical scatterer with sinusoid gain-loss modulation that is subjected to monochromatic oblique waves. We derive an analytical solution to the problem, with which we show how the scatterer parameters, and specifically the modulation phase and incident angle, constitute a real design space for these phenomena.

DOI: 10.1103/PhysRevA.107.023503

I. INTRODUCTION

A judicious design of gain and loss in physical systems in general [1,2] and in particular optical systems [3–8] leads to counterintuitive wave phenomena that are inaccessible by conservative systems. These phenomena, such as supersensitivity [9–11] and unidirectional invisibility [12,13], can be harnessed for different engineering applications that require wave manipulation.

The bulk of the research is on systems that are invariant to combined parity-time ($\mathscr{P}\mathscr{T}$) transformations [14–20], which translates to the condition $\epsilon(-z) = \epsilon^*(z)$ for the dielectric coefficient of a medium that is modulated along z. Depending on the parameters of such systems, their spectrum can be real, in spite of the fact that they are governed by non-Hermitian operators [21,22]. This domain in the parameter space is called the $\mathscr{P}\mathscr{T}$-exact phase, and the rest of the domain, at which the eigenvalues are complex, is called the $\mathscr{P}\mathscr{T}$-broken phase. The transition points between the two phases are a type of *exceptional points* (EPs) [23–27], at which the eigenvalues and eigenvectors become degenerate, and are the source of the counterintuitive phenomena mentioned earlier [28–40].

Of particular relevance to this work is the phenomenon of unidirectional invisibility, which was discovered by Lin *et al.* [12] when analyzing a $\mathscr{P}\mathscr{T}$-symmetric scatterer with sinusoid modulation. Using the rotating wave approximation, they found that at the EPs of the scattering matrix, the reflection vanishes from one side only, while the transmission is unity; they termed it later as anisotropic transmission resonance (ATR) [41]. In addition, the transmission also has zero phase, hence the scatterer is unidirectionally invisible. Later on, Longhi [42], Jones [43], and Uzdin and Moiseyev [44] used exact solutions to analyze the scattering properties beyond the limitations of the rotating wave approximation.

A second pioneering work that motivated the study to follow is by Longhi [45]. He showed that a waveguide with uniform grating and two symmetric layers of gain and loss can simultaneously act as a laser oscillator, emitting coherent waves [46], and as a coherent perfect absorber (CPA), completely absorbing particular incoming waves [47]. Chong *et al.* [48] identified the CPA-laser states as special solutions in the $\mathscr{P}\mathscr{T}$-broken phase, where a pole and a zero of the scattering matrix[1] coincide.

The pioneering works in Refs. [12,45] led to various studies whose objective was to control the phase transition and scattering singularities by different means, such as the incident angle of oblique waves and the chirality in a single gain-loss bilayer [49,50] or the sinusoid modulation properties [51]. Here, we extend the study to the problem of oblique waves that are scattered by waveguides of different sinusoid gain-loss modulations. We derive an exact analytical solution to the problem with which we characterize how the scattering properties, and specifically the EPs, depend on the parameters of the system, such as the incident angle (θ), driving frequency (ω), and the wavelength (β), amplitude, and phase (z_0) of the modulation. For two particular cases where the modulation yields a $\mathscr{P}\mathscr{T}$-symmetric medium, we characterize the $\mathscr{P}\mathscr{T}$ phase diagram in the (θ, ω) and (θ, β) parameter spaces. We also calculate the phase diagram that defines the ATRs in the (θ, β) space. We show that there is a range of modulation amplitudes and wavelengths at which these ATRs coincide with (or reside very close to) Fabry-Pérot resonance frequencies. By analyzing the resultant structure of the phase diagram, we also gain insights on how to access bidirectional zero-reflection states. We conclude the study with an analysis of the poles and zeros of the scattering matrix. We show that the modulation phase and incident angle constitute together real (rather than complex) design space for these singularities and specifically for quasi-CPA-laser states.

Our results are presented in the following order. Section II contains the mathematical formulation of the problem, together with our derivation of its analytical solution. In Sec. III, we recall the two definitions of the scattering matrix and

[1]This scattering matrix is different than the scattering matrix whose EPs correspond to unidirectional invisibility, as detailed later in Sec. III.

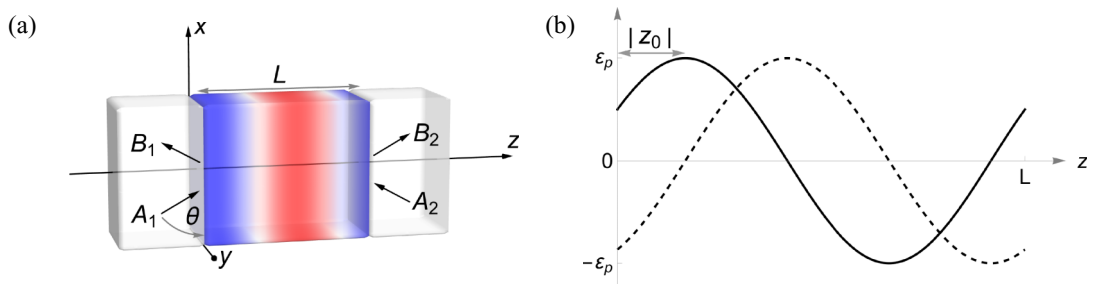

FIG. 1. (a) A nonmagnetic modulated waveguide that is connected to two uniform waveguides at $z = 0$ and L. The coefficients A_1 and A_2 (B_1 and B_2) are identified with the amplitudes of the incoming (outgoing) waves. The dielectric coefficient of the modulated waveguide is $\epsilon(z) = \epsilon_h + \epsilon_p e^{i2\beta(z+z_0)}$. (b) An exemplary modulation profile for some z_0. The continuous and dashed curves correspond to $\mathrm{Re}\,\epsilon$ and $\mathrm{Im}\,\epsilon$, respectively. The last term is also illustrated in the previous panel using the blue-red color map, designating gain and loss, respectively.

their connection to EPs. We further derive a useful relation between the poles and zeros of the two matrix definitions for the particular family of modulations that we analyze. We carry out a parametric study in Sec. IV and conclude this paper with a summary of our main results in Sec. V.

II. PROBLEM STATEMENT AND EXACT SOLUTION

We consider a nonmagnetic medium at $0 \leqslant z \leqslant L$ whose dielectric coefficient is modulated according to

$$\epsilon(z) = \epsilon_h + \epsilon_p e^{i2\beta(z+z_0)}, \tag{1}$$

where $\beta = \pi/L$ is half the wave number of the modulation. Note that when $z_0 = 0$ or $L/2$, the dielectric coefficient satisfies the necessary condition for $\mathscr{PT}$ symmetry, namely, $\epsilon(-z) = \epsilon^*(z)$. (The particular case of $z_0 = 0$ was considered in Refs. [12,42–44] for normal incident waves.) Two homogeneous nonmagnetic waveguides with a dielectric constant ϵ_h are connected at $z \leqslant 0$ and $z \geqslant L$, guiding oblique monochromatic waves to and from the modulated medium (Fig. 1). We focus on TE (or H) modes [52], such that the electric field is in the y direction and propagates in the xz plane. The governing equation for these modes is

$$\left[\partial_x^2 + \partial_z^2 + \frac{\omega^2}{c^2}\epsilon(z)\right]E(x,z) = 0, \tag{2}$$

where c is the speed of light and we consider time dependency of the form $e^{-i\omega t}$ with an angular frequency ω. The solution in the homogeneous waveguides is given by

$$E(x,z) = \begin{cases} A_1 e^{ik_h(x\cos\theta + z\sin\theta)} + B_1 e^{ik_h(x\cos\theta - z\sin\theta)}, & z \leqslant 0, \\ A_2 e^{ik_h[x\cos\theta - (z-L)\sin\theta]} + B_2 e^{ik_h[x\cos\theta + (z-L)\sin\theta]}, & z \geqslant L, \end{cases} \tag{3}$$

where A_1 and A_2 (B_1 and B_2) are the amplitudes of the incoming (outgoing) waves, $k_h = \omega\sqrt{\epsilon_h}/c$, and θ is the angle between the xy plane and the waves in these waveguides.

Inside the modulated medium, we seek solutions in the form

$$E(x,z) = e^{ik_h x\cos\theta} Z(z), \tag{4}$$

where the x dependency is enforced by the continuity of E at $z = 0$ and L. By substituting the ansatz (4) into Eq. (2), we obtain the following equation for $Z(z)$:

$$\left[\partial_z^2 + \frac{\omega^2}{c^2}\left(\epsilon_h + \epsilon_p e^{i2\beta(z+z_0)}\right) - k_h^2\cos^2\theta\right]Z(z) = 0, \tag{5}$$

which can rearranged as

$$\left[\partial_z^2 + k_h^2\sin^2\theta\left(1 + \frac{1}{\sin^2\theta}\frac{\epsilon_p}{\epsilon_h}e^{i2\beta(z+z_0)}\right)\right]Z(z) = 0. \tag{6}$$

Our next step is to rewrite Eq. (6) as a Bessel equation. To this end, we perform a change of variable, namely,

$$\zeta = \sqrt{\frac{k_h^2\epsilon_p}{-\beta^2\epsilon_h}}e^{i\beta(z+z_0)}, \tag{7}$$

such that

$$\partial_z\zeta = i\beta\zeta, \quad \partial_z^2\zeta = -\beta^2\zeta, \tag{8}$$

which together with the chain rule $\partial_z Z = \partial_\zeta Z\partial_z\zeta$ allows us to replace Eq. (6) with

$$\left[\zeta^2\partial_\zeta^2 + \zeta\partial_\zeta + \left(\zeta^2 - \frac{k_h^2}{\beta^2}\sin^2\theta\right)\right]Z = 0. \tag{9}$$

Equation (9) is solved exactly using the Bessel functions $J_{\pm\nu}(\zeta) =: \psi_\pm(z)$, where $\nu = (k_h/\beta)\sin\theta$ is assumed to be a noninteger number. Essentially, Eq. (9) and its solution are generalizations of the results in Refs. [42–44] to oblique waves. The electric field in the modulated medium is a linear combination of these solutions, such that

$$E(x, 0 \leqslant z \leqslant L) = C_1 e^{ik_h x\cos\theta}\psi_+(z) + C_2 e^{ik_h x\cos\theta}\psi_-(z). \tag{10}$$

Our next objective is to relate the amplitudes of the waves inside the modulated medium to the amplitudes in the homogeneous waveguides. To this end, we assemble the two quantities that are continuous along z, i.e., E and $\partial_z E$, into a column vector which we denote by $\mathbf{s}$. In the modulated

medium, this so-called state vector can be written as

$$\mathsf{s}(0 \leqslant z \leqslant L) = \mathsf{Q}(z)\mathsf{c}, \tag{11}$$

where

$$\mathsf{Q}(z) = \begin{pmatrix} \psi_+(z) & \psi_-(z) \\ \partial_z\psi_+(z) & \partial_z\psi_-(z) \end{pmatrix}, \quad \mathsf{c} = \begin{pmatrix} C_1 \\ C_2 \end{pmatrix}.$$

Similarly, the state vector in the right and left ends of the left- and right-homogeneous waveguides is

$$\mathsf{s}(0^-) = \mathsf{Q}_h\mathsf{l}, \quad \mathsf{s}(L^+) = \mathsf{Q}_h\mathsf{r}, \tag{12}$$

respectively, where

$$\mathsf{Q}_h = \begin{pmatrix} 1 & 1 \\ ik_h\sin\theta & -ik_h\sin\theta \end{pmatrix}, \quad \mathsf{l} = \begin{pmatrix} A_1 \\ B_1 \end{pmatrix}, \mathsf{r} = \begin{pmatrix} A_2 \\ B_2 \end{pmatrix}.$$

It now follows from the continuity of the state vector at $z = 0$ and L that

$$\mathsf{Q}_h\mathsf{l} = \mathsf{Q}(0)\mathsf{c}, \ \mathsf{Q}_h\mathsf{r} = \mathsf{Q}(L)\mathsf{c}. \tag{13}$$

Accordingly, the transfer matrix M that relates between the wave amplitudes of the two homogeneous waveguides is

$$\mathsf{M} = \mathsf{Q}_h^{-1}\mathsf{Q}(L)\mathsf{Q}^{-1}(0)\mathsf{Q}_h, \ \text{such that } \mathsf{r} = \mathsf{M}\mathsf{l}; \tag{14}$$

this completes the solution for the electric waves given any amplitude of incoming waves. Using the Bessel's continuation rule we have that $\mathsf{Q}(L) = \mathsf{Q}(0)\begin{pmatrix} e^{ik_h\sin\theta L} & 0 \\ 0 & e^{-ik_h\sin\theta L} \end{pmatrix}$, which together with Eq. (14) yields $\det\mathsf{M} = 1$.

III. SCATTERING ANALYSIS

We can now relate the incoming and outgoing waves in terms of the components of M. One way to do that is

$$\begin{pmatrix} B_1 \\ B_2 \end{pmatrix} = \mathsf{S}\begin{pmatrix} A_1 \\ A_2 \end{pmatrix}, \quad \mathsf{S} = \begin{pmatrix} M_{12}/M_{22} & M_{22}^{-1} \\ M_{22}^{-1} & -M_{21}/M_{22} \end{pmatrix}. \tag{15}$$

If we prescribe an incoming wave with unitary amplitude from the left (right), such that $A_1 = 1$ and $A_2 = 0$ ($A_1 = 0$ and $A_2 = 1$), it follows that the amplitude of the transmitted wave is S_{21} (S_{12}) and the amplitude of the reflected wave is S_{11} (S_{22}). Accordingly, the components of S are identified with the reflection and transmission coefficients, such that

$$\mathsf{S} = \begin{pmatrix} r_L & t \\ t & r_R \end{pmatrix}. \tag{16}$$

The eigenvalues of S are

$$\lambda_{1,2}^{(\mathsf{S})} = \frac{r_L + r_R}{2} \pm \sqrt{\frac{(r_L - r_R)^2}{4} + t^2}; \tag{17}$$

they become degenerate, together with their eigenvectors, when $(r_L - r_R)/t = \pm 2i$. These exceptional points of S for a $\mathscr{P}\mathscr{T}$-symmetric scatterer are linked to the degeneracies in its eigenmodes if it was bounded [53].

There is an alternative scattering matrix, denoted here as $\tilde{\mathsf{S}}$, that is obtained if we interchange the two entries of the column vector in the left-hand side of Eq. (15). By doing so, we obtain

$$\begin{pmatrix} B_2 \\ B_1 \end{pmatrix} = \tilde{\mathsf{S}}\begin{pmatrix} A_1 \\ A_2 \end{pmatrix}, \quad \tilde{\mathsf{S}} = \begin{pmatrix} t & r_R \\ r_L & t \end{pmatrix}. \tag{18}$$

Both Eqs. (15) and (18) deliver the same relations between the incoming and outgoing waves, however, the corresponding scattering matrices have different eigenvalues. Specifically, the eigenvalues of $\tilde{\mathsf{S}}$ are

$$\lambda_{1,2}^{(\tilde{\mathsf{S}})} = t \pm \sqrt{r_L r_R}; \tag{19}$$

they become degenerate when either r_L or r_R vanish. When the scatterer is $\mathscr{P}\mathscr{T}$-symmetric, the exceptional points of $\tilde{\mathsf{S}}$ reflect anisotropic transmission resonances (ATRs), at which the reflection may vanish only from one side while the transmittance is unity since the scattering coefficients for $\mathscr{P}\mathscr{T}$-symmetric system satisfy

$$|T - 1| = \sqrt{R_L R_R}, \tag{20}$$

where $T := |t|^2$ is the transmittance and $R_{L,R} := |r_{L,R}|^2$ are the two reflectances.

The zeros of S, which correspond to a zero eigenvalue, reflect a perfectly absorbing medium, while the poles of S, which correspond to an infinite eigenvalue, reflect a lasing oscillator which emits outgoing coherent waves. It is follows that if S has a zero, then from Eq. (17) we have $t^2 = r_L r_R$, thus $\tilde{\mathsf{S}}$ has a zero as well. In our case, it also follows that if S has a pole then $\tilde{\mathsf{S}}$ has a pole also. To show this, we note that

$$\sigma_1\mathsf{S}^*(-z_0)\sigma_1 = \mathsf{S}^{-1}(z_0), \quad \tilde{\mathsf{S}}^*(-z_0) = \tilde{\mathsf{S}}^{-1}(z_0), \tag{21}$$

where σ_1 is the first Pauli matrix, since $\epsilon(z)$ satisfies Eq. (1). As a result, the product of the modulus of the eigenvalues of $\mathsf{S}(-z_0)$ and $\mathsf{S}(z_0)$ must be 1 and the same holds for $\tilde{\mathsf{S}}$. Therefore, if $\mathsf{S}(z_0)$ has a pole then $\mathsf{S}(-z_0)$ has a zero and hence $\tilde{\mathsf{S}}(-z_0)$ has a zero also, which finally implies that $\tilde{\mathsf{S}}(z_0)$ has a pole. In the next section, we analyze the dependency of the zeros, poles, and EPs of S and $\tilde{\mathsf{S}}$, and the scattering properties on the system parameters and specifically the incident angle.

IV. PARAMETRIC STUDY

In our case study, we set $\epsilon_h = 4$ and study the scattering properties as functions of the remaining parameters of the system. We begin with Fig. 2(a), where we evaluate the logarithm of the transmittance T (solid black) and the logarithm of the two reflectances $R_{L/R}$ (dash-dotted green and dashed blue) as functions of the incident angle θ, setting the rest of the parameters to

$$\xi := \frac{\epsilon_p}{\epsilon_h} = 10^{-1/2}, \quad \frac{\beta}{k_h} = \frac{1}{\sqrt{2}}, z_0 = 0; \tag{22}$$

and recall that since $z_0 = 0$ the scatter is $\mathscr{P}\mathscr{T}$ symmetric. We observe that T varies from 0 at $\theta = 0$ to an anomalous peak of $T = 2.63$ at $\theta = 0.25$. Notably, the reflectance from the right and left are different, where R_L vanishes at $\theta = 0.12$ and $\theta = 0.77$, there the transmittance is unity. These angles correspond to unidirectional reflection that occurs at the EPs of $\tilde{\mathsf{S}}$, as was first reported by Lin *et al.* [12] for the case of normal incident wave. To show this, we plot in Fig. 2(b) the logarithm of the magnitude of $\lambda_{1,2}^{(\tilde{\mathsf{S}})}$ as a function of the incident angle θ. Indeed, we observe that there is a transition from unimodular eigenvalues to nonunimodular eigenvalues at $\theta = 0.12$ and $\theta = 0.77$.

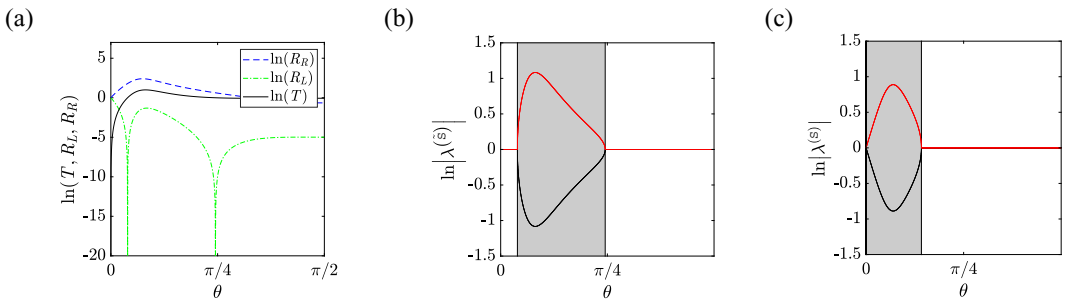

FIG. 2. The case $z_0 = 0$. (a) Logarithm of the transmittance $T = |t|^2$ (solid black) and the two reflectances $R_{L/R} = |r_{L/R}|^2$ (dash-dotted green and dashed blue) as functions of the incident angle θ. (b) Logarithm of the magnitude of $\lambda_{1,2}^{(\tilde{S})}$ as a function of the incident angle θ. (c) Logarithm of the magnitude of $\lambda_{1,2}^{(S)}$ as function of the incident angle. In all panels, $\xi = 10^{-1/2}$ and $\beta/k_h = 2^{-1/2}$.

Ge *et al.* [41] made the observation that, while unidirectional reflectivity occurs at the EPs of $\tilde{\mathsf{S}}$, the EPs of S are those that capture the breaking of the $\mathscr{PT}$ symmetry of the system. These EPs are analyzed in Fig. 2(c) where we evaluate the logarithm of the magnitude of $\lambda_{1,2}^{(\mathsf{S})}$ as a function of the incident angle. We observe that for $0 < \theta < 0.44$, the eigenvalues are nonunimodular and are associated with broken $\mathscr{PT}$ symmetry. $\mathscr{PT}$ symmetry is restored at $\theta = 0.44$ as the eigenvalues become unimodular again. Specifically, both the eigenvalues and eigenvectors coalesce at $\theta = 0.44$, which identifies this angle as the EP of S. Note that, while the modulus of both the eigenvalues is unity beyond this point, the eigenvalues themselves are different. To examine the dependency of the $\mathscr{PT}$ symmetry breaking on the amplitude of the modulation, we evaluate in Fig. 3 the EPs of S for $\xi = 10^{-2}$ (red), 10^{-1} (blue), and $10^{-1/2}$ (green), as functions of $\omega L/c$ [Fig. 3(a)] and β/k_h [Fig. 3(b)]. We highlight the regions that are associated with broken $\mathscr{PT}$ symmetry when $\xi = 10^{-2}$, 10^{-1}, and $10^{-1/2}$ by the light gray, gray, and dark gray, respectively. We observe that, as we increase the amplitude of the perturbation, the region of the broken phase is extended to lower frequencies, or equivalently, greater β/k_h and higher incident angles. Having evaluated the phase diagram of S, we proceed to the phase diagram of $\tilde{\mathsf{S}}$, shown in Fig. 4. Specifically, Figs. 4(a)–4(c) correspond to $\xi = 10^{-2}$ (red), 10^{-1} (blue), and $10^{-1/2}$ (green), respectively. Here, we distinguish between EPs associated with r_L and r_R by light and dark shades, respectively. In contrast to the phase diagram of S, which shows that there is at most one EP for a given ξ and β/k_h, here there could be multiple EPs. For example, there are six EPs when $\xi = 10^{-1}$ and $\beta/k_h = 0.32$ [black vertical line in Fig. 4(b)].

In all the panels, there is a broken region that extends to $\beta/k_h = 1$. Interestingly, this region is bounded from above by the function $\beta = k_h \sin\theta$, which corresponds to the first Fabry-Pérot resonance [54]. In the Appendix, we used a multiple scale expansion to derive an approximated solution under the assumption $\beta \approx k_h \sin\theta$ and that the perturbation is small, resembling the case studied by Lin *et al.* [12]; using this approximation, we show that indeed the scatterer exhibits unidirectional reflection under these assumptions. In fact, all Fabry-Pérot resonances, i.e., $m\beta = k_h \sin\theta$ for any $m \in \mathbb{N}$, provide an approximation for the EPs of $\tilde{\mathsf{S}}$. These approximations for $m = 0 \ldots 10$ are depicted in magenta lines.

The quality of the Fabry-Pérot resonances approximation depends on how small the perturbation and detuning are. To show this, we use our analytical expressions for r_L and r_R [Eqs. (14) to (16)] to find that they are proportional to

$$r_L \propto I_{-(\nu+1)}\left(\nu\sqrt{\tilde{\xi}}\right), \quad r_R \propto I_{-(\nu-1)}\left(\nu\sqrt{\tilde{\xi}}\right), \tag{23}$$

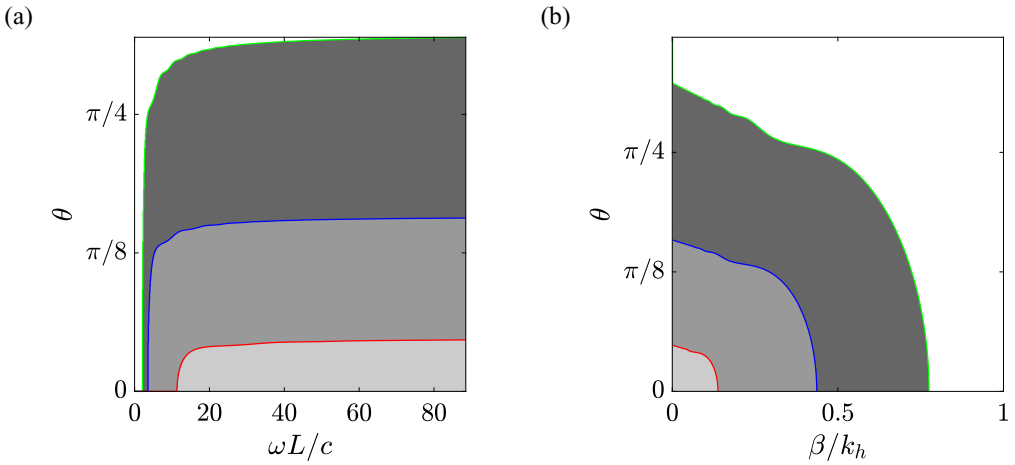

FIG. 3. The case $z_0 = 0$. EPs of S for $\xi = 10^{-2}$ (red), 10^{-1} (blue), and $10^{-1/2}$ (green). as functions of θ versus (a) $\omega L/c$ and (b) β/k_h. Light gray, gray, and dark gray denote the broken phase region of $\xi = 10^{-2}$, 10^{-1}, and $10^{-1/2}$, respectively.

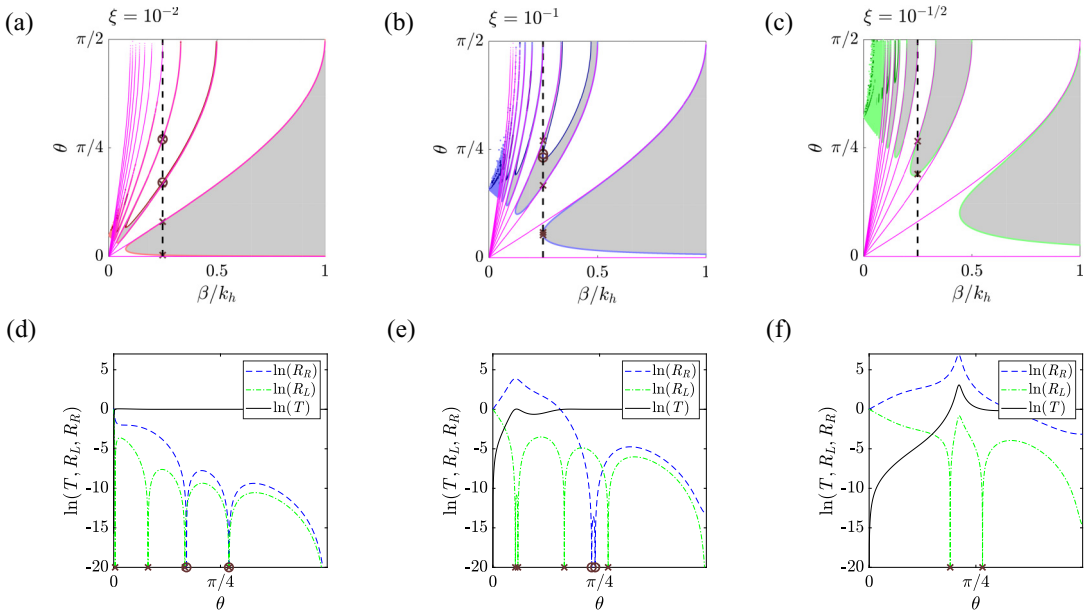

FIG. 4. The case $z_0 = 0$. Phase diagram of $\tilde{\mathsf{S}}$ in the space of $(\theta, \beta/k_h)$ for (a) $\xi = 10^{-1/2}$, (b) $\xi = 10^{-1}$, (c) $\xi = 10^{-2}$. The broken region is denoted in gray and the EPs of $\tilde{\mathsf{S}}$ are highlighted by the colored lines. Panels (d)–(f) show the logarithm of T (solid black) and the two reflectances $R_{L/R}$ (blue, dash-dotted green, and dashed blue) as functions of the incident angle θ for the three different modulations when setting $\beta/k_h = 1/4$.

where I is the modified Bessel function of the first kind and we recall that $\nu = (k_h/\beta)\sin\theta$. The modified Bessel function vanishes in the limit $\tilde{\xi} \to 0^+$ when its order is a nonzero integer, i.e., $\nu \to m \neq 1$, in line with our assumptions. When ν is close to an even (odd) number from above (below), then $I_{-(\nu-1)}$ and $I_{-(\nu+1)}$ vanish for some small positive number. This corresponds to vanishing r_L and r_R at some small perturbation amplitude $\tilde{\xi}$, near a Fabry-Pérot resonance of even (odd) integer. Exceptions for this rule are for (i) I_0, which is nonzero at $\tilde{\xi} = 0$, hence r_R does not vanish in the limit $\nu \to 1$ that is associated with the first Fabry-Pérot resonance ($m = 1$); (ii) when $\nu \to 0^+$, r_R is proportional to I_{1^-}, which does not vanish at some small positive number, hence r_R does not vanish for $m = 0$.

Indeed, we observe that for the smallest modulation [Fig. 4(a)], almost all of the magenta lines coincide with the EPs that we find using the exact solution, including the zeroth order, i.e., when $\theta = 0$. By contrast, for the largest modulation [Fig. 4(c)], the zeroth order does not provide a good approximation at all and the first order begins to coincide with the exact solution only from $\beta/k_h \approx 0.5$.

By analyzing how the zeros of the modified Bessel functions depend on the order, we deduce that the EPs associated with vanishing r_L will always be closer to the Fabry-Pérot resonances than those of vanishing r_R. Since higher Fabry-Pérot resonances become closer in the $(\beta/k_h, \theta)$ space, and the approximated solution improves at smaller modulation amplitude and higher order, the EPs of r_L and r_R become closer at smaller modulations and higher Fabry-Pérot resonances; from a certain frequency they practically coincide. Thus, this trend provides guidelines for achieving bidirectional zero reflection.

To demonstrate this, we evaluate in the remaining panels the logarithm of T (solid black) and the two reflectances $R_{L/R}$ (dash-dotted green and dashed blue) as functions of the incident angle θ for the three different modulations when setting $\beta/k_h = 1/4$. Specifically, Figs. 4(d)–4(f) correspond to $\xi = 10^{-2}$, 10^{-1}, and $10^{-1/2}$, respectively. Figure 4(d) shows that R_L vanishes at $\theta = 0.01$, 0.25, 0.52, and 0.85, as denoted by the cross marks, while R_R vanishes very closely to the later two angles, i.e., near $\theta = 0.52$ and 0.85, as designated by the circle marks. This observation is in agreement with Fig. 4(a), where the wave number ratio $\beta/k_h = 1/4$ is denoted by the dashed line. This line intersects the exceptional line that is near the zeroth Fabry-Pérot resonance at $\theta = 0.01$ and then intersects the exceptional lines that practically coincide with the Fabry-Pérot resonances that are defined by $m = 1$, 2, and 3. Indeed, near Fabry-Pérot resonances for which m equals zero and one, there is no EP that is associated with R_R, while near the higher-order Fabry-Pérot resonances, i.e., two and three, there are pairs of EPs of R_L and R_R that are very close to each other about $\theta = 0.52$ and 0.85. Figure 4(e) shows that R_L vanishes at $\theta = 0.17$, 0.18, 0.53, and 0.85; here, since the modulation amplitude is greater than in Fig. 4(d), the angles at which R_R vanishes, namely, $\theta = 0.73$ and 0.75, are not as close to the nearest angles at which R_L vanishes. Again, these EP observations agree with the way in which the dashed line that denotes $\beta/k_h = 1/4$ intersects the exceptional lines and the Fabry-Pérot resonances. Finally, we see that in Fig. 4(f), which corresponds to the larger modulation amplitude, there are no angles at which R_R vanishes, nor vanishing values R_L near the two lowest-order Fabry-Pérot resonances (zero and one), but only from order two.

The analysis so far was for a zero modulation phase, yielding a $\mathscr{PT}$-symmetric scatterer. We recall that when $z_0 = L/2$, the scatterer is also $\mathscr{PT}$-symmetric: this case is analyzed next. We begin with Fig. 5, which is the same as Fig. 2, only for $z_0 = L/2$. A comparison between Figs. 2(a) and 5(a) shows that while only R_L vanishes (twice) when $z_0 =$

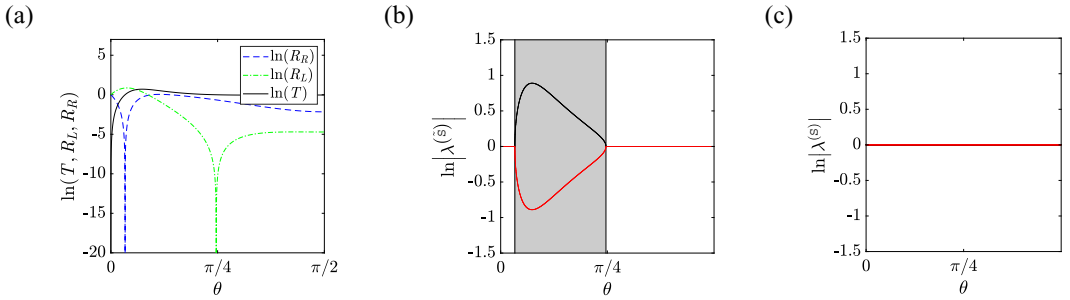

FIG. 5. The case $z_0 = L/2$. (a) Logarithm of the transmittance $T = |t|^2$ (solid black) and the two reflectances $R_{L/R} = |r_{L/R}|^2$ (dash-dotted green and dashed blue) as functions of the incident angle θ. (b) Logarithm of the magnitude of $\lambda_{1,2}^{(\tilde{S})}$ as a function of the incident angle θ. (c) Logarithm of the magnitude of $\lambda_{1,2}^{(S)}$ as a function of the incident angle. In all panels, $\xi = 10^{-1/2}$ and $\beta/k_h = 2^{-1/2}$.

0, when $z_0 = L/2$ both R_L and R_R vanish once, at different angles. A comparison of the remaining two panels in Figs. 2 and 5 shows that, while the broken region of $\tilde{\mathsf{S}}$ is similar for $z_0 = 0$ and $L/2$, the broken region of S is completely different since, when $z_0 = L/2$, S is always at the $\mathscr{PT}$-symmetric phase for the same given scattering parameters. A more complete picture of the difference in the phase diagrams of the two $\mathscr{PT}$-symmetric systems is given next by providing the diagrams that are associated with $z_0 = L/2$. We start with Fig. 6, which shows the EPs of S as functions of θ versus $\omega L/c$ [Figs. 6(a) to 6(c)], and β/k_h [Figs. 6(d) to 6(f)] for $\xi = 10^{-2}$ [red, Figs. 6(a) and 6(d)], 10^{-1} [blue, Figs. 6(b) and 6(e)] and $10^{-1/2}$ [green, Figs. 6(c) and 6(f)], where the broken regions are highlighted with gray. A comparison with the diagram of $z_0 = 0$ (Fig. 3) shows that $z_0 = L/2$ has a much richer diagram, exhibiting multiple reentries to the broken region when either one of the three parameters (θ, ω, and β) is varied. This is in sharp contrast with a single entry when $z_0 = 0$. In addition, when $z_0 = 0$, the broken region of the greater modulations encloses the broken region of the smaller modulations, while when $z_0 = L/2$, there are regions that belong to the broken phase of smaller modulations, while belonging to the exact phase of greater modulations.

In Fig. 7 we also evaluate the phase diagram of $\tilde{\mathsf{S}}$ in the $(\theta, \beta/k_h)$ space; Figs. 7(a) to 7(c) correspond to $\xi = 10^{-2}$, 10^{-1}, and $10^{-1/2}$, where the EPs are highlighted in red, blue, and green, respectively, and the broken regions are in gray. We distinguish between the EPs that are associated with zero r_L and r_R by light and dark shades, respectively. There is some similarity with the diagram of $z_0 = 0$, however, here the structure is more complicated and the broken regions are larger.

Here again, all Fabry-Pérot resonances provide an approximation for the EPs of $\tilde{\mathsf{S}}$ and these approximations for $m = 0 \ldots 10$ are depicted in magenta lines. Now we find that the expressions for r_L and r_R are proportional to the Bessel

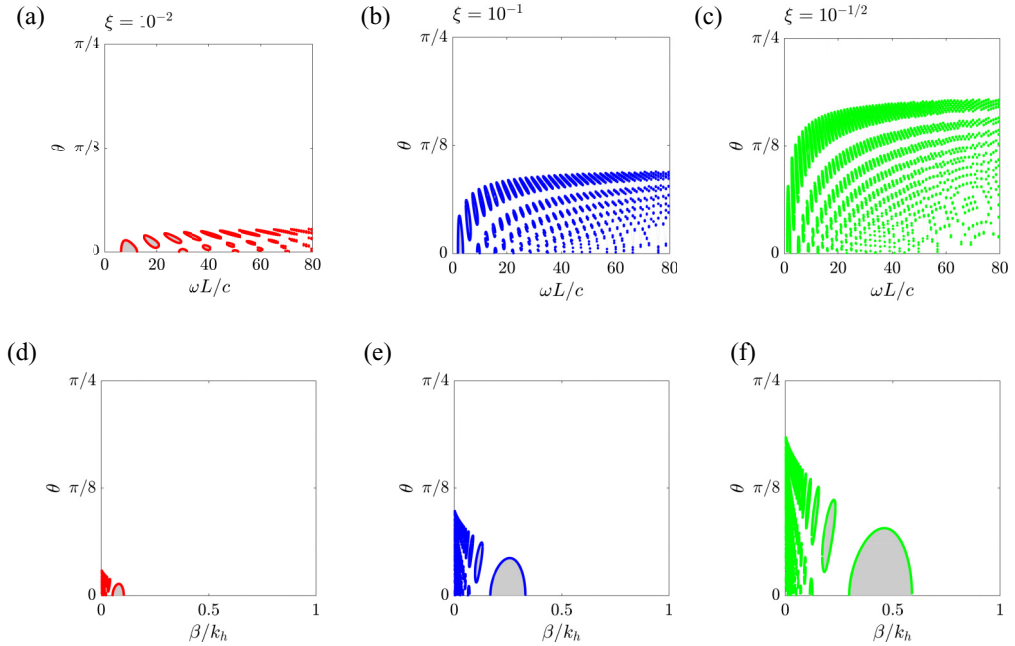

FIG. 6. The case $z_0 = L/2$. Phase diagram of S in the $(\theta, \omega L/c)$ (a)–(c) space and (d)–(f) $(\theta, \beta/k_h)$ space for (a), (d) $\xi = 10^{-1/2}$, (b), (e) $\xi = 10^{-1}$, and (c), (f) $\xi = 10^{-2}$. The broken region is denoted in gray and the EPs of S are highlighted by the colored lines.

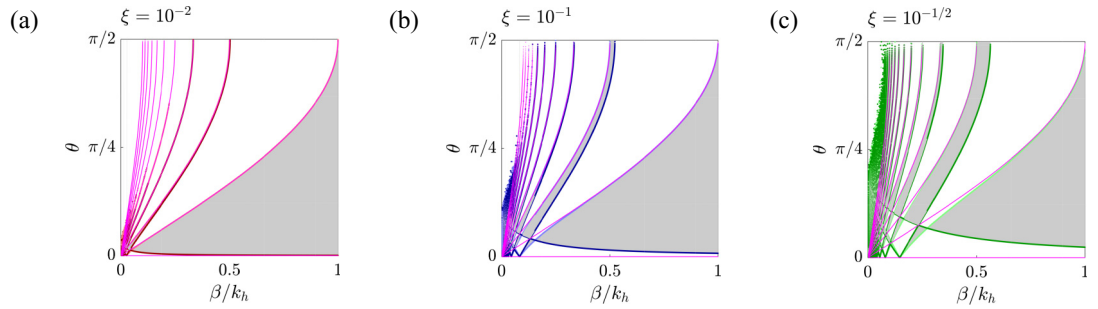

FIG. 7. Phase diagram of $\tilde{\mathsf{S}}(z_0/L = 1/2)$ in the space of $(\theta, \beta/k_h)$ for (a) $\xi = 10^{-1/2}$, (b) $\xi = 10^{-1}$, (c) $\xi = 10^{-2}$. The broken region is denoted in gray and the EPs of $\tilde{\mathsf{S}}$ are highlighted by the colored lines.

functions

$$r_L \propto J_{-(\nu+1)}\left(\nu\sqrt{\tilde{\xi}}\right), \quad r_R \propto J_{-(\nu-1)}\left(\nu\sqrt{\tilde{\xi}}\right)J_{(\nu-1)}\left(\nu\sqrt{\tilde{\xi}}\right). \tag{24}$$

In contrast with the behavior of the modified Bessel functions in Eq. (23), the Bessel functions in Eq. (24) vanish at some positive argument when ν approaches to a positive integer number from below. This corresponds to vanishing r_L and r_R at some small perturbation amplitude $\tilde{\xi}$ near a Fabry-Pérot resonance. Here there is only one exception to this rule, namely, that r_R does not vanish in the limit $\nu \to 1$, which is associated with the first Fabry-Pérot resonance, i.e., $m = 1$.

We proceed to analyze scatterers that do not satisfy $\mathscr{PT}$ symmetry by considering three exemplary values of z_0 that are different from 0 and $L/2$. This is carried out in Fig. 8, where we evaluate the logarithm of T and $R_{L/R}$ as functions of θ, setting $\xi = 10^{-1/2}$ and $\beta/k_h = 2^{-1/2}$. Specifically, Figs. 8(a)–8(c) correspond to $z_0 = -1/10$, $3/10$, and $-2/5$, respectively. While R_L vanish near $\theta = \pi/4$ in all the panels (corresponding to $\nu = 1$), overall there is a strong variation in the scattering properties from one z_0 to another. For example, when $z_0/L = -1/10$, T peaks at $\theta = 0.57$ to 1.34, and then decays to 1.01 at $\theta = \pi/2$. By contrast, when $z_0/L = 3/10$, T peaks at $\theta = 0.82$ to 1.11, and then decays to 1.04 at $\theta = \pi/2$. Furthermore, when $z_0/L = -1/10$, R_L is unity at $\theta = 0$, decays to 0.09 at $\theta = 0.13$ which is a local minimum, then peaks to 0.14 at $\theta = 0.29$ and then decays to zero at $\theta = 0.78$, and increases again to 0.01 at $\theta = \pi/2$. By contrast, when $z_0/L = 3/10$, the peaks of R_L is at $\theta = 0$ from which it decays to zero at $\theta = 0.79$ and increases again to 0.01 at $\theta = \pi/2$. The most interesting result is observed for $z_0/L = -2/5$ about $\theta = 0.09$, where T, R_R, and R_L all peak to giant values at the order of 10^4. The extreme scattering values in the later case hint at the existence of a pole of the scattering matrix near $z_0/L = -2/5$ and $\theta = 0.09$. This observation motivates us to evaluate the eigenvalues of the scattering matrix eigenvalues in the $(\theta, z_0/L)$ space. By doing so, we can identify the poles and zeros of the scattering matrix, which we plot in Fig. 9 using black circles and red crosses, respectively, for $\xi = 10^{-2}$ [Fig. 9(a)], 10^{-1} [Fig. 9(b)], and $10^{-1/2}$ [Fig. 9(c)], when $\beta/k_h = 1/30$. We observe that the poles and zeros are distributed symmetrically with respect to the $\mathscr{PT}$-symmetric perturbation $z_0 = 0$, namely, if at a certain (z_0, θ) pair there is a pole (zero) then at $(-z_0, \theta)$ there is a zero (pole). This is in accordance with our analysis in Sec. III, where we showed that product of the modulus of the eigenvalues of $\mathsf{S}(-z_0)$ and $\mathsf{S}(z_0)$ is 1. Such distribution is similar to the symmetric distribution of poles and zeros in the complex frequency plane that was studied by Ge *et al.* [41]. There, this distribution resulted from the $\mathscr{PT}$ symmetry of the medium, while in our case, it is a consequence of Eq. (21).

A comparison of the different panels in Fig. 9 shows that by increasing the amplitude of the modulation, the number of poles and zeros increases as well. The collection of all these points constitutes an arc-like structure whose tip is associated with the angle at which $\mathscr{PT}$ transition occurs for the $\mathscr{PT}$-symmetric system defined by $z_0 = 0$. To show this, we evaluate the logarithm of the eigenvalues of S when $z_0 = 0$ as function of θ. Specifically, Figs. 9(d) to 9(f) correspond to $\xi = 10^{-2}$, 10^{-1}, and $10^{-1/2}$, respectively; we highlight the broken region at which the eigenvalues are nonunimodular by gray. Indeed, we observe how the tip of the arc-like structure and the transition angle from gray to white coincide. While

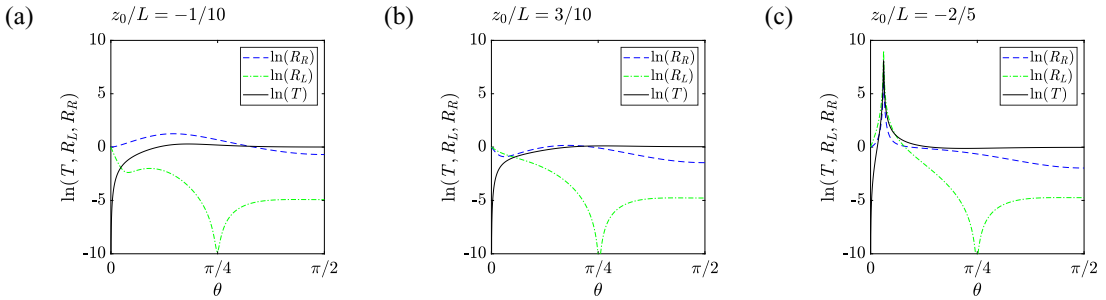

FIG. 8. The transmittance $T = |t|^2$ (solid black), reflectance from the left $R_L = |r_L|^2$ (dash-dotted green), and reflectance from the right $R_R = |r_R|^2$ (dashed blue) as functions of the incident angle for $\xi = 10^{-1/2}$, $\beta/k_h = 2^{-1/2}$, and z_0/L equals (a) $-1/10$, (b) $3/10$, and (c) $-2/5$.

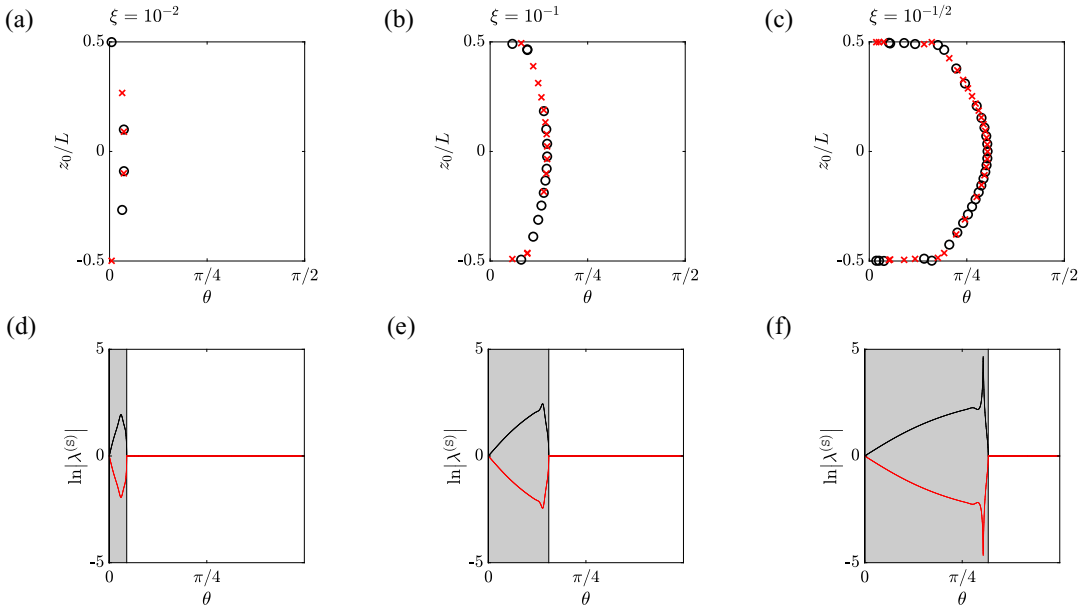

FIG. 9. Poles (black circles) and zeros (red crosses) of the scattering matrix in the $(z_0/L, \theta)$ space for $\beta/k_h = 1/30$ and (a) $\xi = 10^{-2}$, (b) 10^{-1}, and (c) $10^{-1/2}$. Logarithm of the eigenvalues of S as function of θ for (d) $\xi = 10^{-2}$, (e) 10^{-1}, and (f) $10^{-1/2}$; we highlight the broken region at which the eigenvalues are nonunimodular by gray.

we are unable to derive a mathematical explanation for this observation, we note that similar observations were made in Refs. [41,48], which were later explained in Ref. [53]. Specifically, Fig. 8 in Ref. [41] showed that at the phase transition of the S matrix there is an anticrossing of the poles in the complex frequency plane, see also Fig. 3 in Ref. [48]. There, the symmetric distribution of the poles and zeros about the imaginary axis is a result of the $\mathscr{P}\mathscr{T}$ symmetry of the system; here, the (θ, z_0) space plays a similar role, where the symmetric distribution of the poles and zeros is about $z_0 = 0$, owing to Eq. (21).

Figure 9(f) also displays a divergence of the eigenvalues, as one of them tends to explode and the other tends to vanish. This is in accordance with the proximity of a zero and a pole near $z_0 = 0$ in Fig. 9(c), where we recall that their overlap corresponds to CPA-laser states. We thus refer to these states, where a zero and pole are very close but not coincide, as a quasi-CPA-laser state. In such states, as we highlight next, one of the eigenvalues tends to vanish, but remains greater from zero, while the other grows significantly, but remains finite. This behavior of the eigenvalues implies that the scatterer can simultaneously absorb almost completely incoming coherent waves and significantly enhance certain incoherent excitations.

Quasi-CPA-laser states occur also, e.g., for $\xi = 10^{-2}$ at $\theta \approx 0.12$, when $z_0/L \approx \pm 0.1$. We examine in Fig. 10 how the logarithm of the eigenvalues modulus of S vary near these states as a function of two different variables: (i) z_0/L when theta is fixed to ≈ 0.12 [Fig. 10(a)] and (ii) θ when z_0/L is fixed to $z_0 \approx 0.1$ [Fig. 10(b)], while the rest of the parameters are set to $\beta/k_h = 1/30$ and $\xi = 10^{-2}$. We observe in Fig. 10(a) the symmetric distribution of each one of the eigenvalues with respect to $z_0 = 0$. In addition, we observe how near $z_0/L \approx -0.1$ one of them grows and the other diminishes, where near $z_0/L \approx 0.1$ their tendency is interchanged. The rapid growth and decay of the eigenvalues near the critical angle $\theta \approx 0.12$ is demonstrated in Fig. 10(b).

V. SUMMARY

We derived an exact solution to the problem of monochromatic oblique TE waves that are scattered by a waveguide with sinusoid gain-loss modulation. We analyzed a family of modulations that are parametrized by their phase, amplitude, and wavelength. We investigated how these parameters, together with the frequency and incident angle of the waves, affect the emergence of lasing, perfect absorption, and anisotropic transmission resonances. For two particular modulations that satisfy $\mathscr{P}\mathscr{T}$ symmetry, we evaluated the diagram of the exact and broken $\mathscr{P}\mathscr{T}$ phases in the parameter space and the phase diagram that defines the anisotropic transmission resonances. The two modulations have different diagrams, one of which is much richer, exhibiting multiple re-entries to the broken

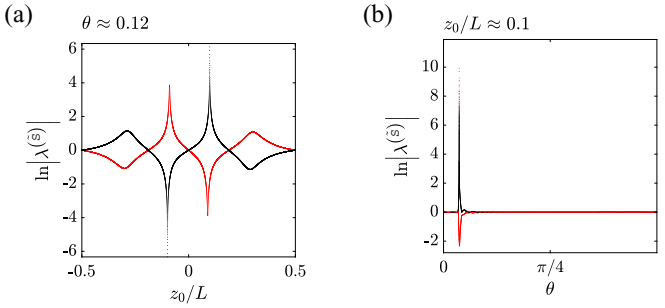

FIG. 10. Logarithm of the modulus of the eigenvalues of $\tilde{\mathsf{S}}(\xi = 10^{-2})$ (a) as a function of the phase with fixed incident angle $\theta \approx 0.12$ and (b) as a function of the incident angle with fixed phase $z_0 \approx 0.1$.

region. With regard to the diagrams of the anisotropic transmission resonances, we showed that there is a regime in the parameter space where these resonances reside very close to Fabry-Pérot resonances. A further investigation of this property has provided guidelines on how to design bidirectional zero-reflection states. Finally, we analyzed the poles and zeros of the scattering matrix, which correspond, respectively, to lasing and perfect absorption states. We showed that the the modulation phase and incident angle constitute a design space for these singularities when the scatterer is subjected to monochromatic waves. Specifically, we identified quasi-CPA-laser states when a zero and pole are very close but do not coincide. These states correspond to scatterers that can simultaneously absorb almost completely the incoming coherent waves and significantly enhance certain incoherent excitations.

ACKNOWLEDGMENTS

We thank anonymous reviewers for constructive feedback that helped us improve this paper. This project was funded by the European Union (ERC, EXCEPTIONAL, Project No. 101045494).

APPENDIX: APPROXIMATED SOLUTION NEAR THE FIRST FABRY-PÉROT RESONANCE

Lin *et al.* [12] showed that, for normal incident waves ($\theta = \pi/2$) impinging on a $\mathscr{P}\mathscr{T}$-symmetric Bragg scatterer, the scattering matrix $\tilde{\mathsf{S}}$ exhibits an EP at the Bragg point. Here, using a multiple scale expansion, we show a similar result for oblique waves, impinging on a non-Hermitian scatterer exhibiting one period of modulation, where the EP occurs at the first Fabry-Pérot resonance, i.e., $\beta = k_h \sin\theta$. To show this, we assume that the detuning $\delta := \beta - k_h \sin\theta$ is very small relatively to the perturbation wave number. We further assume that the amplitude of the perturbation is small, such that $\tilde{\xi} := \xi/\sin^2\theta \ll 1$. With these assumptions at hand, we introduce the variables $z^{(1)} := z$ and $z^{(2)} := \tilde{\xi} z$, and employ a power expansion of Z in the form

$$Z = Z^{(1)} + \tilde{\xi} Z^{(2)} + \cdots, \tag{A1}$$

to solve Eq. (6). Upon substituting Eq. (A1) into Eq. (6), using the transformation $\partial_z = \partial_{(1)} + \tilde{\xi}\partial_{(2)}$, we obtain two equations

$$\partial^2_{(1)} Z^{(1)} + \beta^2 Z^{(1)} = 0, \tag{A2}$$

$$\partial^2_{(1)} Z^{(2)} + \beta^2 Z^{(2)} = \left(\frac{\beta^2 - (k_h \sin\theta)^2}{\tilde{\xi}} - k_h^2 \frac{\xi}{\tilde{\xi}} e^{2i\beta(z+z_0)} \right) \times Z^{(1)} - 2\partial_{(1)}\partial_{(2)} Z^{(1)}, \tag{A3}$$

for the orders $\mathscr{O}(1)$ and $\mathscr{O}(\tilde{\xi})$, respectively. The solution of Eq. (A2) for the leading order is

$$Z^{(1)} = A_f(z^{(2)}) e^{i\beta z^{(1)}} + B_b(z^{(2)}) e^{-i\beta z^{(1)}},$$

and to determine A_f and B_b we require that the secular terms in Eq. (A3) vanish [55]. This provides

$$\partial_{(1)} \begin{pmatrix} A_f \\ B_b \end{pmatrix} = \begin{pmatrix} \frac{\delta}{i} & k_h^2 \frac{\xi}{-2ik_h \sin\theta} e^{2i\beta z_0} \\ 0 & -\frac{\delta}{i} \end{pmatrix} \begin{pmatrix} A_f \\ B_b \end{pmatrix}. \tag{A4}$$

The solution of Eq. (A4) is

$$\begin{pmatrix} A_f \\ B_b \end{pmatrix} = \left[\cos(\delta z) \begin{pmatrix} 1 & 0 \\ 0 & 1 \end{pmatrix} + i \frac{\sin(\delta z)}{\delta} \begin{pmatrix} -\delta & k_h^2 \frac{\xi}{2k_h \sin\theta} e^{2i\beta z_0} \\ 0 & \delta \end{pmatrix} \right] \begin{pmatrix} A_f(0) \\ B_b(0) \end{pmatrix}. \tag{A5}$$

Following the standard procedure to calculate T and $R_{L/R}$, we obtain

$$T = 1, R_R = \frac{k_h^4 \frac{\xi^2}{4(k_h \sin\theta)^2}}{|\delta \cot(\delta L)|^2 + \delta^2}, R_L = 0, \tag{A6}$$

which indeed implies that, under the foregoing assumptions, there is unidirectional reflection that is associated with an EP of $\tilde{\mathsf{S}}$.

[1] Y. Ashida, Z. Gong, and M. Ueda, Non-hermitian physics, Adv. Phys. **69**, 249 (2020).
[2] R. El-Ganainy, K. G. Makris, M. Khajavikhan, Z. H. Musslimani, S. Rotter, and D. N. Christodoulides, Non-Hermitian physics and $\mathscr{P}\mathscr{T}$ symmetry, Nat. Phys. **14**, 11 (2018).
[3] R. El-Ganainy, M. Khajavikhan, D. N. Christodoulides, and Ş. K. Özdemir, The dawn of non-Hermitian optics, Commun. Phys. **2**, 37 (2019).
[4] L. Feng, R. El-Ganainy, and L. Ge, Non-Hermitian photonics based on parity–time symmetry, Nat. Photonics **11**, 752 (2017).
[5] B. Midya, H. Zhao, and L. Feng, Non-Hermitian photonics promises exceptional topology of light, Nat. Commun. **9**, 2674 (2018).
[6] Ş. K. Özdemir, S. Rotter, F. Nori, and L. Yang, Parity–time symmetry and exceptional points in photonics, Nat. Mater. **18**, 783 (2019).
[7] E. Pilehvar, E. Amooghorban, and M. K. Moravvej-Farshi, Oblique propagation of the squeezed states of s(p)-polarized light through non-hermitian multilayered structures, Opt. Express **30**, 3553 (2022).
[8] H. Zhao and L. Feng, Parity–time symmetric photonics, Natl. Sci. Rev. **5**, 183 (2018).
[9] P. Djorwe, Y. Pennec, and B. Djafari-Rouhani, Exceptional Point Enhances Sensitivity of Optomechanical Mass Sensors, Phys. Rev. Appl. **12**, 024002 (2019).
[10] J. Wiersig, Enhancing the Sensitivity of Frequency and Energy Splitting Detection by Using Exceptional Points: Application to Microcavity Sensors for Single-Particle Detection, Phys. Rev. Lett. **112**, 203901 (2014).
[11] Q. Zhong, J. Ren, M. Khajavikhan, D. N. Christodoulides, Ş. K. Özdemir, and R. El-Ganainy, Sensing with Exceptional Surfaces in Order to Combine Sensitivity with Robustness, Phys. Rev. Lett. **122**, 153902 (2019).
[12] Z. Lin, H. Ramezani, T. Eichelkraut, T. Kottos, H. Cao, and D. N. Christodoulides, Unidirectional Invisibility Induced by $\mathscr{P}\mathscr{T}$-Symmetric Periodic Structures, Phys. Rev. Lett. **106**, 213901 (2011).

[13] A. Mostafazadeh, Invisibility and $\mathscr{P}\mathscr{T}$ symmetry, Phys. Rev. A **87**, 012103 (2013).

[14] C. M. Bender and S. Boettcher, Real Spectra in Non-Hermitian Hamiltonians Having $\mathscr{P}\mathscr{T}$ Symmetry, Phys. Rev. Lett. **80**, 5243 (1998).

[15] J. Christensen, M. Willatzen, V. R. Velasco, and M.-H. Lu, Parity-Time Synthetic Phononic Media, Phys. Rev. Lett. **116**, 207601 (2016).

[16] D. Christodoulides *et al.*, *Parity-Time Symmetry and its Aapplications* (Springer, New York, 2018), Vol. 280.

[17] R. Fleury, D. Sounas, and A. Alù, An invisible acoustic sensor based on parity-time symmetry, Nat. Commun. **6**, 5905 (2015).

[18] E.-M. Graefe and H. F. Jones, $\mathscr{P}\mathscr{T}$-symmetric sinusoidal optical lattices at the symmetry-breaking threshold, Phys. Rev. A **84**, 013818 (2011).

[19] Z. Hou, H. Ni, and B. Assouar, $\mathscr{P}\mathscr{T}$-Symmetry for Elastic Negative Refraction, Phys. Rev. Appl. **10**, 044071 (2018).

[20] C. E. Rüter, K. G. Makris, R. El-Ganainy, D. N. Christodoulides, M. Segev, and D. Kip, Observation of parity–time symmetry in optics, Nat. Phys. **6**, 192 (2010).

[21] N. Moiseyev, *Non-Hermitian Quantum Mechanics* (Cambridge University Press, Cambridge, England, 2011).

[22] A. Mostafazadeh, Pseudo-hermiticity versus $\mathscr{P}\mathscr{T}$ symmetry: The necessary condition for the reality of the spectrum of a non-hermitian hamiltonian, J. Math. Phys. **43**, 205 (2002).

[23] M. V. Berry, Physics of non-Hermitian degeneracies, Czech. J. Phys. **54**, 1039 (2004).

[24] D. Heiss, Circling exceptional points, Nat. Phys. **12**, 823 (2016).

[25] W. D. Heiss, The physics of exceptional points, J. Phys. A: Math. Theor. **45**, 444016 (2012).

[26] A. A. Mailybaev, O. N. Kirillov, and A. P. Seyranian, Geometric phase around exceptional points, Phys. Rev. A **72**, 014104 (2005).

[27] M.-A. Miri and A. Alù, Exceptional points in optics and photonics, Science **363**, eaar7709 (2019).

[28] V. Achilleos, G. Theocharis, O. Richoux, and V. Pagneux, Non-Hermitian acoustic metamaterials: Role of exceptional points in sound absorption, Phys. Rev. B **95**, 144303 (2017).

[29] G. Elbaz, A. Pick, N. Moiseyev, and G. Shmuel, Encircling exceptional points of bloch waves: mode conversion and anomalous scattering, J. Phys. D **55**, 235301 (2022).

[30] L. Geng, W. Zhang, X. Zhang, and X. Zhou, Topological mode switching in modulated structures with dynamic encircling of an exceptional point, Proc. R. Soc. A **477**, 20200766 (2021).

[31] T. Goldzak, A. A. Mailybaev, and N. Moiseyev, Light Stops at Exceptional Points, Phys. Rev. Lett. **120**, 013901 (2018).

[32] H. Hodaei, A. U. Hassan, S. Wittek, H. Garcia-Gracia, R. El-Ganainy, D. N. Christodoulides, and M. Khajavikhan, Enhanced sensitivity at higher-order exceptional points, Nature (London) **548**, 187 (2017).

[33] S. Longhi, Exceptional points and photonic catastrophe, Opt. Lett. **43**, 2929 (2018).

[34] B. Lustig, G. Elbaz, A. Muhafra, and G. Shmuel, Anomalous energy transport in laminates with exceptional points, J. Mech. Phys. Solids **133**, 103719 (2019).

[35] B. Peng, Ş. K. Özdemir, M. Liertzer, W. Chen, J. Kramer, H. Yılmaz, J. Wiersig, S. Rotter, and L. Yang, Chiral modes and directional lasing at exceptional points, Proc. Natl. Acad. Sci. **113**, 6845 (2016).

[36] A. Pick, Z. Lin, W. Jin, and A. W. Rodriguez, Enhanced nonlinear frequency conversion and purcell enhancement at exceptional points, Phys. Rev. B **96**, 224303 (2017).

[37] C. Shen, J. Li, X. Peng, and S. A. Cummer, Synthetic exceptional points and unidirectional zero reflection in non-hermitian acoustic systems, Phys. Rev. Mater. **2**, 125203 (2018).

[38] C. Shi, M. Dubois, Y. Chen, L. Cheng, H. Ramezani, Y. Wang, and X. Zhang, Accessing the exceptional points of parity-time symmetric acoustics, Nat. Commun. **7**, 11110 (2016).

[39] W. R. Sweeney, C. W. Hsu, S. Rotter, and A. D. Stone, Perfectly Absorbing Exceptional Points and Chiral Absorbers, Phys. Rev. Lett. **122**, 093901 (2019).

[40] X. Yin and X. Zhang, Unidirectional light propagation at exceptional points, Nat. Mater. **12**, 175 (2013).

[41] L. Ge, Y. D. Chong, and A. D. Stone, Conservation relations and anisotropic transmission resonances in one-dimensional $\mathscr{P}\mathscr{T}$-symmetric photonic heterostructures, Phys. Rev. A **85**, 023802 (2012).

[42] S. Longhi, Invisibility in $\mathscr{P}\mathscr{T}$-symmetric complex crystals, J. Phys. A: Math. Theor. **44**, 485302 (2011).

[43] H. F. Jones, Analytic results for a pt-symmetric optical structure, J. Phys. A: Math. Theor. **45**, 135306 (2012).

[44] R. Uzdin and N. Moiseyev, Scattering from a waveguide by cycling a non-hermitian degeneracy, Phys. Rev. A **85**, 031804(R) (2012).

[45] S. Longhi, $\mathscr{P}\mathscr{T}$-symmetric laser absorber, Phys. Rev. A **82**, 031801(R) (2010).

[46] A. E. Siegman, *Lasers* (University Science Books, Mill Valley, CA, 1986).

[47] Y. D. Chong, L. Ge, H. Cao, and A. D. Stone, Coherent Perfect Absorbers: Time-Reversed Lasers, Phys. Rev. Lett. **105**, 053901 (2010).

[48] Y. D. Chong, L. Ge, and A. D. Stone, $\mathscr{P}\mathscr{T}$-Symmetry Breaking and Laser-Absorber Modes in Optical Scattering Systems, Phys. Rev. Lett. **106**, 093902 (2011).

[49] S. Droulias, I. Katsantonis, M. Kafesaki, C. M. Soukoulis, and E. N. Economou, Accessible phases via wave impedance engineering with $\mathscr{P}\mathscr{T}$-symmetric metamaterials, Phys. Rev. B **100**, 205133 (2019).

[50] I. Katsantonis, S. Droulias, C. M. Soukoulis, E. N. Economou, and M. Kafesaki, $\mathscr{P}\mathscr{T}$-symmetric chiral metamaterials: asymmetric effects and $\mathscr{P}\mathscr{T}$-phase control, Phys. Rev. B **101**, 214109 (2020).

[51] Q. Liu, C. Qin, B. Wang, and P. Lu, Scattering singularities of optical waveguides under complex modulation, Phys. Rev. A **101**, 033818 (2020).

[52] T. Tamir, H. C. Wang, and A. A. Oliner, Wave propagation in sinusoidally stratified dielectric media, IEEE Trans. Microwave Theory Tech. **12**, 323 (1964).

[53] P. Ambichl, K. G. Makris, L. Ge, Y. Chong, A. D. Stone, and S. Rotter, Breaking of $\mathscr{P}\mathscr{T}$ Symmetry in Bounded and Unbounded Scattering Systems, Phys. Rev. X **3**, 041030 (2013).

[54] N. Hodgson and H. Weber, *Optical Resonators: Fundamentals, Advanced Concepts, Applications*, Springer Series in Optical Sciences (Springer, New York, 2005).

[55] R. G. Watts, Introduction to perturbation methods, In *Essentials of Applied Mathematics for Engineers and Scientists* (Springer, New York, 2012), pp. 153–162.